3

Fluorescent X-Ray Computed Tomography Using Synchrotron Radiation Towards Molecular Imaging

Tetsuya Yuasa[1] and Tohoru Takeda[2]
[1]*Yamagata University,*
[2]*Kitasato University,*
Japan

1. Introduction

Presently, nuclear imaging techniques such as positron emission tomography (PET), and single photon emission CT (SPECT) are quite vital tools in clinical medicine as molecular imaging modalities to investigate the cause, diagnosis and therapy of diseases, e.g., Alzheimer's disease, Parkinson's disease, ischemic heart disease, cardiomyopathy and cancer, from the viewpoint of molecule. On the other hand, recent advance in genetic engineering have generated rodent models of human diseases that afford important clues to their causes, diagnoses and treatment. Studies using mouse and rat as the animal models have become important in most areas, such in molecular biology, toxicology, and drug discovery research. Hypotheses about the onset of disease and the effectiveness of treatment can be tested with the animals before terminal studies for human. Mice and rats have become key animal models for the study of development of human disease. They offer the possibility to manipulate their genome and produce accurate models of many human disorders resulting in significant progress in the understandings of human diseases. Also here, the molecular imaging techniques are quite important tools for observing the physiological and pathological status in vivo. However, they still suffer from insufficient spatial resolution. In addition, they must require radio-active imaging agency, resulting in being an intractable measurement method. So, the invention of a novel molecular imaging technique using non-radioactive imaging agencies with high-contrast and high spatial resolutions has been eagerly waited for.

X-ray fluorescence analysis (XRF) is one of the most sensitive physicochemical analysis methods to identify trace elements with high sensitivity and high quantitativeness by detecting the fluorescent x-ray emitted from them. Use of synchrotron x-ray as the light source empowers it to detect trace elements with much higher sensitivity, because synchrotron x-ray has some excellent properties for XRF. Then, fluorescent x-ray scanning tomography (FXST) has been developed based on XRF to investigate a 2-dimensional distributions of specific elements. SR-FXST at the first stage was employed in planar mode to evaluate very low contents of medium- or high-atomic-number trace elements up to the pictograms range (Iida & Gohshi, 1991; Takeda, et al., 1995). However, this method is

usually limited to scanning either the surface of the object or thin slices of samples with a perpendicular x-ray beam. Fluorescent x-ray computed tomography (FXCT) method combining SR-XRF with computed tomography technique bypasses this restriction. Hogan et al. (Hogan et al., 1991) theoretically discussed this approach and we were the first to implement it by using synchrotron radiation (Takeda, et al., 1996; —, 1998).

SR-FXCT enables us to establish a low-invasive or non-destructive cross-sectional imaging method for biomedical use at high sensitivity and at high spatial resolution. The SR-FXCT is being developed to depict the distribution of specific elements inside the biomedical object (Takeda, et al., 2000; —, 2001). So far, we have successfully imaged myocardinal fatty acid metabolism of cardiomyopathic animal model ex vivo (Thet-Thet-Lwin, et al., 2007; —, 2008), and cerebral perfusion of small rodents ex vivo (Takeda et al., 2009) after injecting non-radioactive iodine labeled cerebral perfusion agent (IMP), and fatty acid metabolic agent (BMIPP), respectively.

Although SR-FXCT allows sub-millimeter resolution, this approach is hampered by the long measurement time required, as conventional FXCT is based on the first generation type of computed tomography (CT), which acquires a set of projections by translational and rotational scans using pencil-beam geometry. In order to complete the measurements during the course of anesthesia, the number of projections and the data acquisition time for each data point need to be reduced, resulting in a reduction in image quality. Thus, just a few slices can be obtained for in vivo imaging of a rat head, while under anesthesia (Takeda, et al., 2009). Therefore, conventional FXCT cannot substitute for PET or SPECT, which can obtain 3-D tomographic images. In order to overcome the difficulty, the parallel data acquisition scheme has been proposed (Huo, et al., 2008; —, 2009).

This chapter is organized as follows. In Section 2, we present some background materials on SR-FXCT. Section 3 first describes SR-FXCT of the first generation based on pencil-beam geometry in its imaging protocol, reconstruction method, and applications, then points out the difficulty to prevent the SR-FXCT from being a molecular imaging modality. A novel type of SR-FXCT based on sheet-beam geometry for overcoming the difficulty is presented in Sections 4. Section 5 discusses the imaging properties of the SR-FXCT based on experimental results. Finally, some concluding remarks are given in Section 6.

2. Backgrounds

In this section, we will introduce the fundamental items indispensable for discussion in the following sections.

2.1 Fluorescent X-ray

When materials are exposed by short-wavelength x-rays or gamma rays, photoelectric effect will take place. The photoelectric effect is a phenomenon in which electrons are emitted from matter after the absorption of energy from electromagnetic radiation. With the removal of an electron in this way, the electronic structure of the atom is unstable, and electrons in higher orbitals "fall" into the lower orbital to fill the hole left behind. In falling, energy is released in the form of a photon, the energy of which is equal to the energy difference of the two orbitals involved. Thus, the fluorescence x-rays will be emitted isotropically (Fig. 1).

There are a limited number of ways in which this can happen, L→K transition is called K_α, an M→K transition is called K_β, an M→L transition is called L_α, and so on (Fig. 2). Since each element has characteristic energy of electronic orbitals, the kind of elements can be investigated by analyzing fluorescent x-ray energy. Furthermore, the intensity of each characteristic radiation is proportional to the amount of elements, so the amount of elements can be investigated from the intensity.

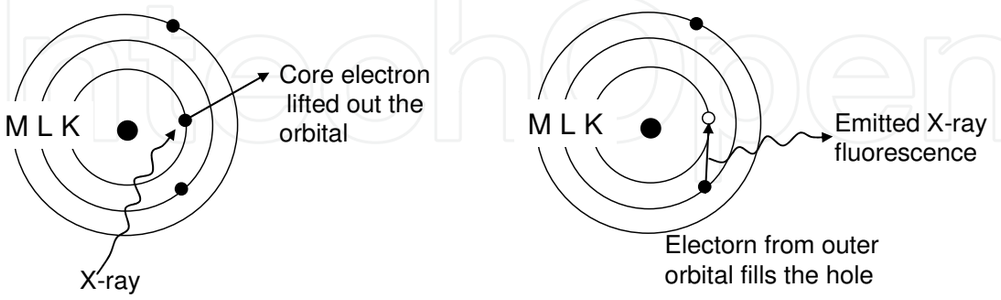

Fig. 1. Emission of fluorescent x ray

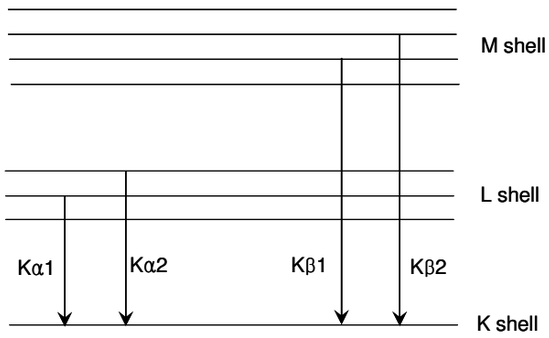

Fig. 2. Characteristics of fluorescent x rays

X-ray fluorescence analysis (XRF) is one of the most sensitive physicochemical analysis methods to identify trace elements with high sensitivity by detecting the fluorescent x ray emitted from them. Use of synchrotron x ray as the light source empowers it to detect trace elements with much higher sensitivity, because synchrotron x-ray has some excellent properties for XRF. In addition, combining XRF with computed tomography technique enable us to establish a low-invasive or non-destructive cross-sectional imaging method for biomedical use at high sensitivity and at high spatial resolution.

2.2 Synchrotron radiation

Synchrotron radiation is electromagnetic radiation from electrons accelerated to high speed in several stages to achieve a final energy that is typically in the GeV range. Then, the electrons are forced to travel in a closed path in a storage ring by strong magnetic fields of a few T. The synchrotron radiation is projected at a tangent to the electron storage ring and captured as beamlines. These beamlines may originate at bending magnets, which mark the corners of the storage ring; or insertion devices, which are located in the straight sections of the storage ring. Beamline is consisted by some optical devices which control the bandwidth, photon flux, beam dimensions, focus, and collimation of the rays.

The synchrotron radiation has some excellent properties as follows:

A. High brightness and high intensity, many orders of magnitude larger than those of x-rays produced by conventional x-ray tubes.
B. High level of polarization (linear or elliptical).
C. High collimation, i.e. small angular divergence of the beam.
D. Low emittance, i.e. the product of source cross section and solid angle of emission is small.
E. Wide tunability in energy/wavelength by monochromatization (sub eV up to the MeV range).
F. High brilliance, exceeding other natural and artificial light sources by many orders of magnitude.

The major applications of synchrotron light are in condensed matter physics, materials science, biology and medicine.

2.3 Computed tomography

In 1972, the first viable computed tomography (CT) scanner was invented by Honsfield using x rays, which can be used to investigate the structures inside bodies with various planes or even as volumetric (3D) representations. Here, we consider a 2-dimensional case using parallel incident beams. We introduce the typical coordinate systems for CT measurements. The *xy*- and *st*-coordinate systems are fixed to the object and the incident ray, as shown in Fig. 3, respectively. Here, the *st*-coordinate system is obtained by rotating the *xy*-coordinate system by θ about the origin in the counter-clockwise direction. X-ray CT is a technique for probing the attenuation coefficient of an object by use of multiple x rays. Each ray is assumed to travel through the object without changing its direction. Measured quantity at each point is described as

$$I_t(s,\theta) = I_o \, \mathrm{e}^{\int_{R(s,\theta)} \mu(x,y)\, dl} \tag{1}$$

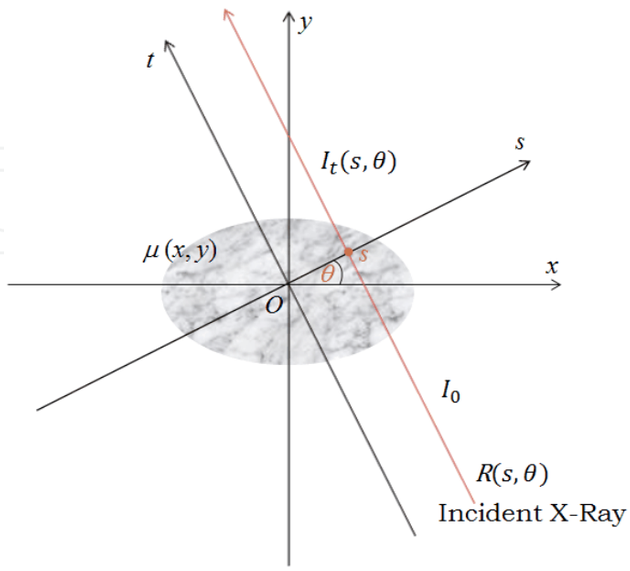

Fig. 3. CT geometry

using the Beer's law. Here, I_t and I_o are the transmitted and the incident x-ray intensities, respectively: μ is a distribution of linear attenuation coefficients, and the shoulder of exponential function means a line integral of μ along the linear trajectory of the incident x ray, $R(s,\theta)$.

In order to reconstruct 2-D function $\mu(x, y)$, we need the line integral along the x-ray path with respect to r and θ. By taking logarithm against Eq. (1), we obtain line integrals, i.e., projections. Projections along multiple x rays in multiple directions are measured. Then, applying a reconstruction algorithm to the projections, such as the filtered backprojection method, the distribution of the attenuation coefficient $\mu(x, y)$ is to be estimated. Here, we notice that the measurements required for CT reconstruction are not x-ray transmittance but the line integral. Therefore, CT measurement is a measurement protocol to systematically collect a series of line integrals of quantity of interest from multiple directions.

2.4 Fluorescent X-ray computed tomography using synchrotron radiation

Fluorescent x-ray computed tomography is a hybrid technique between XRF, which is a physicochemical analysis with high sensitivity and high quantitativeness, and CT, which obtains inside information non-destructively. We give a rough sketch of FXCT here, while the quantitative consideration is given in the next section.

Suppose that a beam of monochromatic x ray is incident on an object containing specific element such as iodine. The advantageous properties of synchrotron radiation for fluorescent x-ray analysis are its broad energy spectrum that allows beam energy tunableness, its high brightness, and its natural forwardly collimation, as described in section 2.2. Thereby, we obtain a high-quality parallel monochromatic beam as an incident beam. The atoms locating on the beam path isotropically emit fluorescent x-ray photons having energy peculiar to the element according to their concentration. Since the amount of fluorescent x-ray photons from each site on the beam path depends on the concentration of the element, we can obtain the line integral of the concentration by acquiring the fluorescent photons efficiently and precisely. For this purpose, we must consider the problem where and how the detector should be set.

We aggressively utilize a linear polarization property of SR. SR is linearly polarized in the plane of the electron storage ring. Ideally, Compton scattered radiation, which is dominant as noise source in hard x-ray regions, is not emitted in a direction at a right angle to the incident beam in the polarization plane (Yuasa et al., 1997; —, 1997). Therefore, the polarized nature of SR allows the maximal reduction of the spectral background originating from Compton scattering in the plane of the storage ring by positioning the detector at 90 degrees to the beam in the plane of the polarization. Preparing an ideal detector having a detective surface with infinitely thin height and infinitely long width, we achieve the objective.

As aforementioned, we can collect the fluorescent x-ray photons with high signal to noise ratio using SR as an incident beam. Projections are acquired at constant angular steps using a translation-rotation motion of the object over 180 degrees.

3. SR-FXCT based on pencil beam geometry

The x-ray fluorescence analysis method has been used in tracer element detection studies, with sensitivities reaching one picogram per gram of certain elements (Iida & Gohshi, 1991).

However, these measurements require a thin sample and, therefore, are limited to measurements near the surface. Then, fluorescent x-ray scanning tomography was developed in order to investigate spatial distributions of specific elements. Fluorescent x-ray scanning tomography employing an x-ray tube has been used to study iodine in samples of several millimeters in diameter (Cesareo & Mascarenhas, 1989), while x-ray fluorescence scanning microtomography employing synchrotron radiation has been used in studies of Fe and Ti in 8-mm samples and in the detection of iron in a bee head (Boisseau & Grodzins, 1987). However, 2-dimensionally scanning a sample is time-consuming. In addition, since the scanning tomography also requires a thin sample, spatial distributions of specific elements in a massive sample cannot be measured (Recently, in order to obtain 3-dimensional tomogram, scanning tomography using a confocal collimator was proposed (Chukalina, et al., 2007)). In order to overcome the problems, Hogan et al. proposed an imaging scheme based on CT concept (Hogan, et al., 1991).

3.1 SR-FXCT imaging system with pencil beam geometry

The schematic diagram of a typical SR-FXCT system of the first generation is shown in Fig. 4. A white x-ray beam from a source is monochromatized using a monochromator, which in our system is a two-crystal Bragg–Bragg device employing Si crystals. It is collimated into a thin beam using a slit before impinging on the subject. Fluorescent x ray is emitted isotropically by the de-exciting contrast atoms along the line of the incident beam, with intensity proportional to the product of the iodine concentration in the incident beam and the incident x-ray flux rate. It is detected in a solid state detector (an HPGe detector) operating in a photon-counting mode. While in this article FXCT from a single kind of imaging agent is discussed, different FXCT images from multiple kinds of imaging agents can be simultaneously obtained by setting the corresponding energy windows (Yu, et al., 2001; Golosio, et al., 2003; Deng, et al., 2007; —, 2011). The detector is collimated to reduce the amount of stray radiation being detected, and is positioned perpendicular to the incident

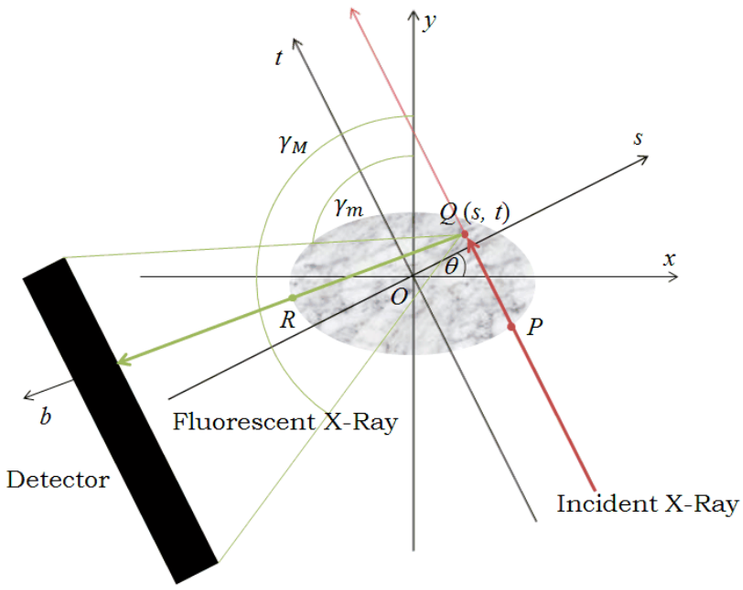

Fig. 4. CT geometry

beam for reducing the Compton scattering background in the spectrum. The energy of the incident beam is carefully tuned so that the fluorescent spectral line does not overlap with the Compton scatter peak. Despite these precautions, the detected signal contains some scattered photons.

In studies of phantom and plant (Simionovici, et al., 2000; —, 2001) and sediment particles, micro-FXCT images were obtained with a spatial resolution of less than 0.01 mm. Our FXCT system, designed for biomedical study, improved the spatial resolution from 1 mm to 0.025 mm. Compared with recent molecular imaging techniques such as micro-PET (positron emission tomography) and micro-SPECT (single photon emission computed tomography), FXCT has the advantage of not requiring the use of a radioactive agent limiting easy preparation of the object (Takeda, et al., 2001). In addition, FXCT has high quantitativeness.

3.2 Principle and formulation

The principles of the fluorescent X-ray CT is depicted in Fig. 4 (Hogan, et al., 1991; Yuasa, et al., 1997). The coordinate system (x, y) is fixed in the reference frame of the sample. The system (s, t) is represents the rotating coordinate system associated with the specimen, and they are related to system (x, y) by a rotation of an angel θ. The two coordinate systems are connected in the relationship as follows:

$$\begin{aligned} s &= x\cos\theta + y\sin\theta \\ t &= -x\sin\theta + y\cos\theta \end{aligned} \tag{2}$$

The points P, Q, and R represent the intersection of the incident x-ray beam with the object's surface, the point of interest, and an intersection of a single emitted fluorescent x-ray with the object's surface, respectively. An incident x-ray with an initial intensity I_0 travels through the point P, and arrives at the point Q, and then fluorescent emitted isotropically x ray from the iodine atoms excited at the point Q. The interaction of the beam with the object can be depicted with three steps in the following:

Step 1: Incident radiation travels from P to Q while receiving attenuation by the object. The process for a single ray at position s and projection angle θ can be given by

$$I_1(s,\theta) = I_0 \exp(-\int_{-\infty}^{t} \mu^I(s,t')dt') \tag{3}$$

where I_0 is the intensity of incident beam and $\mu^I(s,t)$ is the linear absorption coefficient for the energy of the incident x-ray. The integration proceeds along the line segment PQ.

Step 2: The fluorescent x-ray fluxes are emitted isotropically at position Q in quantity proportional to the product of the incident intensity and the concentration of imaging agents $d(s, t)$. The fluorescent x-ray emitted fluxes from the point Q, I_2 can be given by

$$I_2 = \mu_{ph} \cdot \omega \cdot \Omega(s,t) \cdot I_0 \exp(-\int_{-\infty}^{t} \mu^I(s,t')dt')d(s,t)\Delta t \tag{4}$$

where μ_{ph} is the photoelectric linear attenuation coefficient, ω is the fluorescent yield of the K_α emission, Ω is the solid angle from the source to the detector and Δt is the differential of t.

Step3: The fluorescent flux travels from Q to the detective surface while receiving attenuation by the object. It reaches the detector with a flux rate give by

$$\mu_{ph} \cdot \omega \cdot \Omega(s,t) \cdot I_0 \exp(-\int_{-\infty}^{t} \mu^I(s,t')dt')d(s,t) \cdot \exp\left(-\int_0^{\infty} \mu^F(s - b\cos\gamma, s + b\sin\gamma)db\right)\Delta t \tag{5}$$

γ ($\gamma_m \le \gamma \le \gamma_M$) denotes the angle between a single ray inside the fan-shaped emitted fluorescence photon and the *t*-axis (Fig. 4) and $\mu^F(s,t)$ is the linear attenuation coefficient of fluorescent x rays. Integration from γ_m to γ_M with respect to γ yields the flux rate of the fluorescent x ray I_3, detected by a detector is given by

$$I_3 = \mu_{ph}\omega\Omega(s,t)I_0 \exp(-\int_{-\infty}^{t} \mu^I(s,t')dt')d(s,t) \cdot \int_{\gamma_m}^{\gamma_M} \exp\left(-\int_0^{\infty} \mu^F(s - b\cos\gamma, s + b\sin\gamma)db\right)d\gamma\Delta t \tag{6}$$

The total fluorescent flux to the detective surface I, is obtained by integrating I_3 with respect to t from negative infinity to positive infinity.

$$\begin{aligned} I(\theta,s) &= \mu_{ph} \cdot \gamma \cdot \Omega \cdot I_0 \int_{-\infty}^{+\infty} \exp(-\int_{-\infty}^{u} \mu^I(s,t')dt') \cdot d(s,t) \\ &\quad \cdot \int_{\gamma_m}^{\gamma_M} \exp(-\int_0^{\infty} \mu^F(s - b\cos\gamma, s + b\sin\gamma)db)d\gamma dt \\ &= \int_{-\infty}^{+\infty} f(\theta,s,t) \cdot g(\theta,s,t) \cdot d(s,t)dt \end{aligned} \tag{7}$$

where,

$$f(\theta,s,t) = I_0 \exp(-\int_{-\infty}^{u} \mu^I(s,t')dt') \tag{8}$$

and

$$g(\theta,s,t) = \mu_{ph}\omega \int_{\gamma_m}^{\gamma_M} \exp\left[-\int_0^{\infty} \mu^F(s - b\cos\gamma, s + b\sin\gamma)db\right]d\gamma \tag{9}$$

The $f(\theta,s,u)$ represents the incident radiation intensity attenuated reaches the point Q, and $g(\theta,s,u)$ represents the fluorescent radiation intensity attenuated were detected by a detector, respectively. The goal of image reconstruction in FXCT is to solve the $d(s, u)$. We can estimate the $d(s, u)$ from eq. (7) when the distributions of the linear attenuation coefficients of the object at the energies of the incident and fluorescent x-ray, $\mu^I(s,u)$ and $\mu^F(s,u)$ are known.

3.3 Reconstruction

As seen in the previous section, the measurement process is relatively complicated. So, analytical solutions may not be available without some approximation (Hogan, et al., 1991;

Brunetti, et al., 2001; La Riviere, 2004; Miqueles, et al. 2010). To numerically solve (7), we need to discretize it. The object is assumed to be two dimensional. Here, we adopt the *xy*-coordinate system fixed to the object for discretization. Three matrices, d_j, μ^I_j and , μ^F_j (j = 1, 2, …, N) fixed to the *xy*-coordinate system are prepared, corresponding to the functions $d(s, t)$, $\mu^I(s, t)$ and $\mu^F(s, t)$, where j (j = 1, 2, …, N) is the index identifying the pixel. Note that μ^I_j and μ^F_j are known. Also, let us number each incident x-ray S_i with the index i that runs from 1 to M. S_i is then the set consisting of the indexes identifying pixels which are intersected by the ith ray (Fig. 5). Taking note of the jth pixel being struck by beam S_i, let us follow the process described in the previous section using Fig. 6.

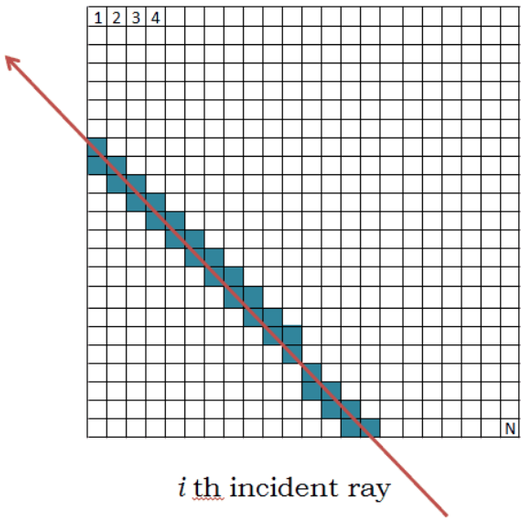

Fig. 5. Example of a set S_i defined for the ith incident X-ray.

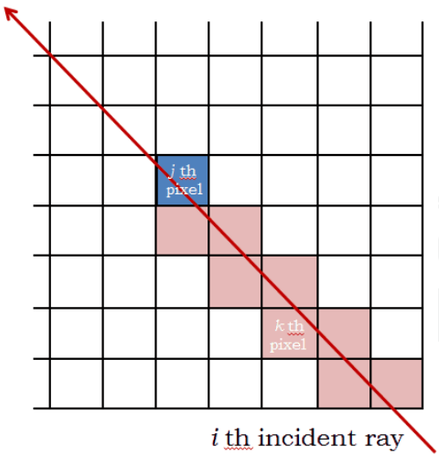

Fig. 6. Example of a set S_{ij} defined for the ith incident X-ray and the jth pixel.

Step 1: The incident x-ray is attenuated by the shaded pixels in Fig. 6. Here, S_{ij} is defined as the set of the indices denoting these pixels, which is apparently the subset of the set S_i. Defining the length of the line segment such that the ith xray is intersected with the kth pixel ($k \in S_{ij}$) as L^I_{ik}, the incident x-ray dose in front of the ith pixel is written in the form

$$f_{ij} = I_0 \exp\left(-\sum_{k \in S_{ij}} \mu_k^I L_{ik}^I \right) \tag{10}$$

which corresponds to (8).

Step 2: The fluorescent x-ray is radiated isotropically, whose absorbed flux rate is in proportion to the product of the flux rate of the x-ray entering the *j*th pixel and concerning this phenomenon, $\omega \mu_{ph} f_{ij} L^I_{ij}$, and the iodine concentration, d_j. Let us define the angle at which the *j*th pixel is viewed by the detector as δ (Fig. 7). The x-ray absorbed flux rate corresponding to (4) is $(\delta / 2\pi)\ \omega \mu_{ph} f_{ij} L^I_{ij} d_j$.

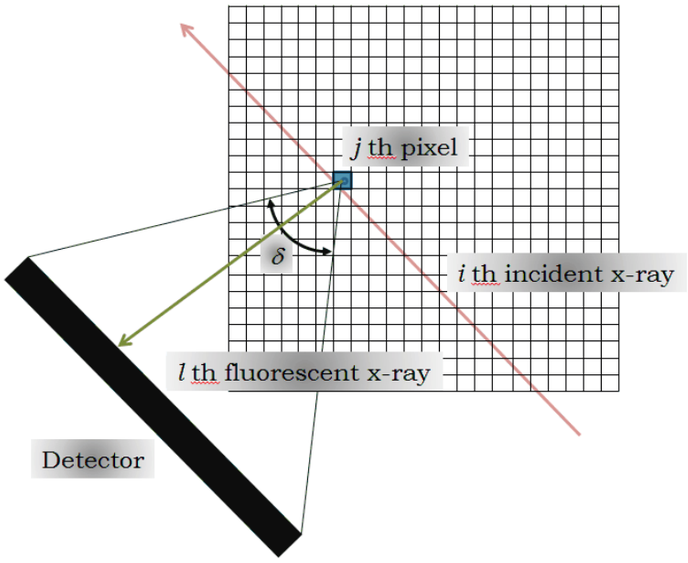

Fig. 7. Definition of angle δ.

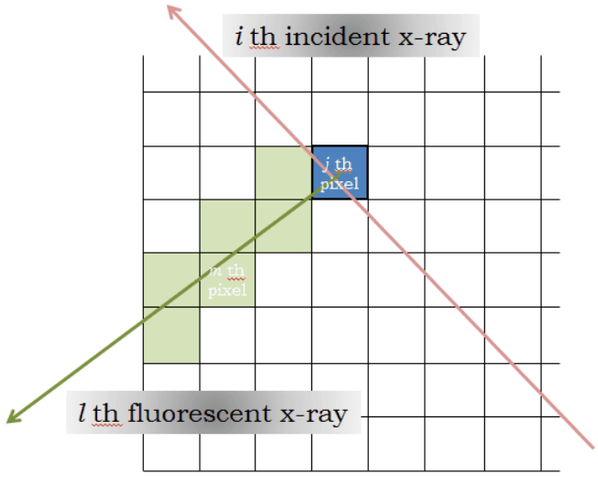

Fig. 8. Example of a set T_{ijl} defined for the *i*th incident X-ray and the *j*th pixel and the *l*th fluorescent X-ray.

Step 3: We consider the attenuation process up to the detector. For a predefined integer, K, let $\Delta\delta = \delta / K$. Here, the fan-shaped fluorescent x-ray is approximated by K individual x-rays. We define the index identifying the angle of the fluorescent x-rays as l ($1 \le l \le K$). Considering the jth pixel ($j \in S_i$) and the lth fluorescent x-ray, we consider the attenuation from the lth ray from the jth pixel to the detector (Fig. 8). Let T_{ijl} be a set of indexes consisting of the pixels which are intersected with the lth fluorescent x-ray. These pixels, denoted as the shaded pixels in Fig. 8, attenuate the lth fluorescence x-ray before they reach the detector. Let L^F_{ijm} be the length of the line segment such that the lth ray is intersected with the mth pixel ($m \in T_{ijl}$). The lth ray is subject to the attenuation by

$$\exp\left(- \sum_{m \in T_{ijl}} \mu^F_m L^F_{ijm} \right)$$

Hence, the discretized representation corresponding to (9) is

$$g_{ij} = \mu_{ph} \omega \frac{\Delta\delta}{2\pi} \sum_{l=1}^{K} \exp\left(- \sum_{m \in T_{ijl}} \mu^F_m L^F_{ijm} \right) \tag{11}$$

Accordingly, the discretization of (7) yields

$$\begin{aligned} I_i &= \sum_{j \in S_i} f_{ij} g_{ij} L^I_{ij} d_j \\ &= \sum_{j \in S_i} h_{ij} d_j \end{aligned} \tag{12}$$

where

$$h_{ij} = f_{ij} g_{ij} L^I_{ij} \tag{13}$$

The matrix representation of (12) is

$$\boldsymbol{I} = \boldsymbol{H}\boldsymbol{d} \tag{14}$$

where

$$\boldsymbol{H} = \left(h_{ij} \right) \qquad \left(1 \le i \le M, 1 \le j \le N \right) \tag{15}$$

$$\boldsymbol{I} = \left(I_i \right) \qquad \left(1 \le i \le M \right) \tag{16}$$

and

$$\boldsymbol{d} = \left(d_j \right) \qquad \left(1 \le j \le N \right) \tag{17}$$

As a result, in order to reconstruct a cross section, you should solve the matrix equation. A variety of approaches were proposed (Chukalina, et al., 2002; Golosio, et al., 2003; Miqueles,

et al., 2011; La Riviere, et al., 2010). If data amount is not so huge, you may solve it through a direct matrix calculation. If so, you should take an iterative reconstruction method. In addition, if a signal to noise ratio is not high, you should select a statistical reconstruction method such as EM algorithm (Rust, et al., 1998). On the other hand, while we discussed reconstruction when distributions of μ^I and μ^F are known, in order to obtain these distributions additional CT measurements are required. Approaches to circumvent this problem have been proposed (Schroer, et al., 2001; La Riviere, et al., 2006; —, 2006;).

3.4 Imaging experiments

Here, we introduce the actual experimental results, which show that SR-FXCT has high sensitivity and spatial resolution as well as quantitativeness, and offers useful knowledges to biomedical sciences.

3.4.1 Imaging setup

The experiment was carried out at the bending magnet beam line BLNE-5A in KEK, Japan (Fig. 9). The photon flux rate in front of the subject was approximately 10^8 photons/mm^2/sec at a beam current of 40 mA with 6.5 GeV. The FXCT system consists of a

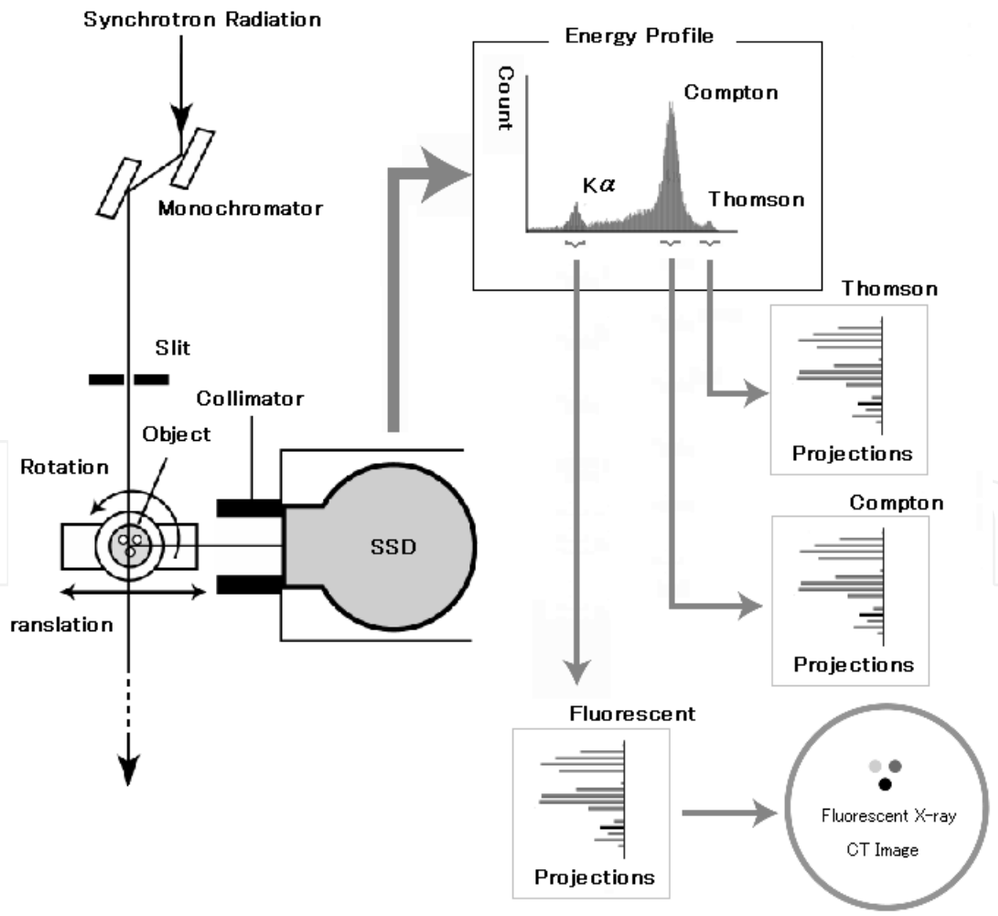

Fig. 9. Schematic of fluorescent x-ray CT system

silicon (220) double-crystal monochromator, an x-ray slit system, a scanning table for the target object, a highly purified germanium (HPGe) detector (IGRET, EG&G Ortec, USA) with a parallel collimator, two pindiode detectors and a computer system. The white x-ray beam was monochromated at 37 keV using the silicon double-crystal monochromator. The incident monochromatic x-ray beam was collimated into a pencil beam with square cross section (0.25 mm × 0.5 mm) using the x-ray slit system. Fluorescent x-rays were detected by the HPGe detector in photon-counting mode. To reduce the amount of Compton radiation captured by the detector, the HPGe detector was positioned perpendicular to the incident monochromatic x-ray beam. The data-acquisition time of the HPGe detector was set a few seconds. An example of energy profile acquired at a data point by the imaging system is shown in Fig. 10. We can observe three peaks, i.e., the iodine-fluorescence, the Compton, and the Thomson peaks. The net counts in an energy window centered at the characteristic x-ray fluorescent spectral line of 28.3 keV at each projection point constitute the CT projections. Projections are acquired at constant angular steps using a translation-rotation motion of the subject over 180 degrees in a conventional CT configuration. Also, the imaging setup can simultaneously obtain Compton scatter CT image as well as FXCT image, because the measurement process of Compton scatter is the same as that of fluorescent x-ray (Yuasa, et al., 1997; Golosio, et al., 2003). Although through this article synchrotron x ray is supposed as incident beam, currently a bench-top FXCT system using a diagnostic energy range polychromatic (i.e. 110 kVp) pencil-beam source is being developed (Cheong, et al., 2010; Jones, et al., 2011).

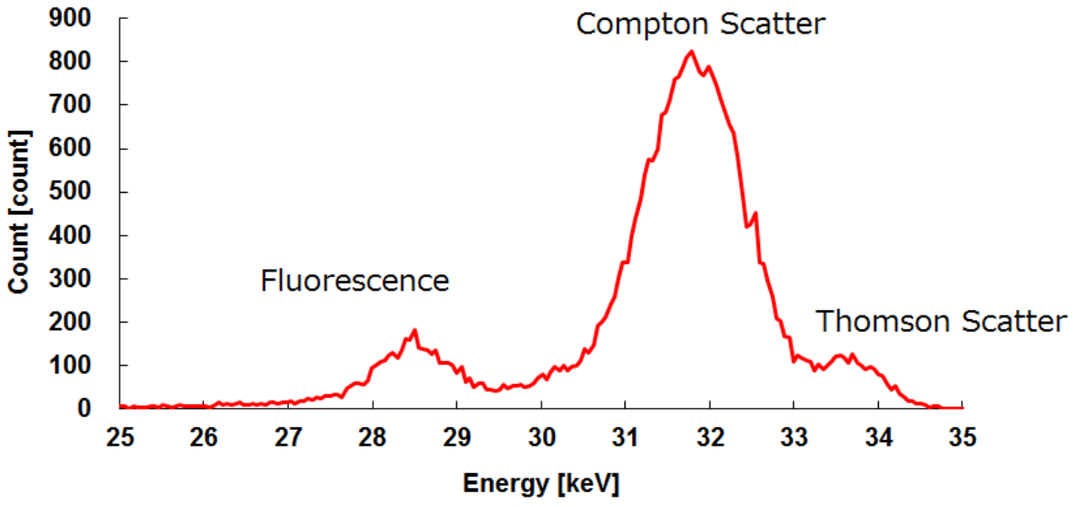

Fig. 10. Schematic of fluorescent x-ray CT system

The experiments for evaluating quantitativeness of SR-FXCT were performed using a 10 mm-diameter acrylic phantom with 3 mm holes to evaluate the contrast detectability corresponding to iodine concentrations of 200, 100, 50, 25 and 15 mg ml^{-1} (Fig. 11). Using the contrast-resolution phantom, we confirmed that the FXCT could visualize a 0.005 mg ml^{-1} iodine solution at 0.25 mm in-plane spatial resolution and 0.5 mm slice thickness. There was an excellent linear correlation between pixel value in the FXCT image and the iodine concentration (Fig. 12). From this graph we observed satisfactory quantitativeness and thus estimated the iodine concentration for a given image count.

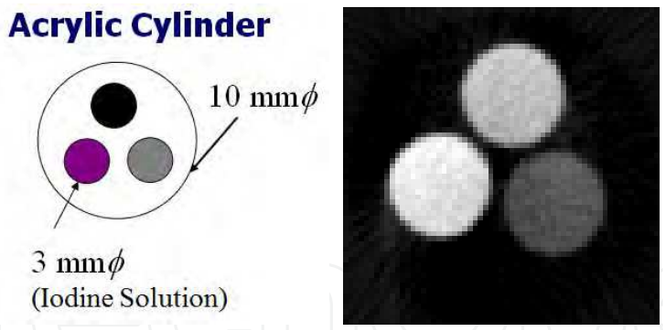

Fig. 11. Acrylic phantom and an example of FXCT image.

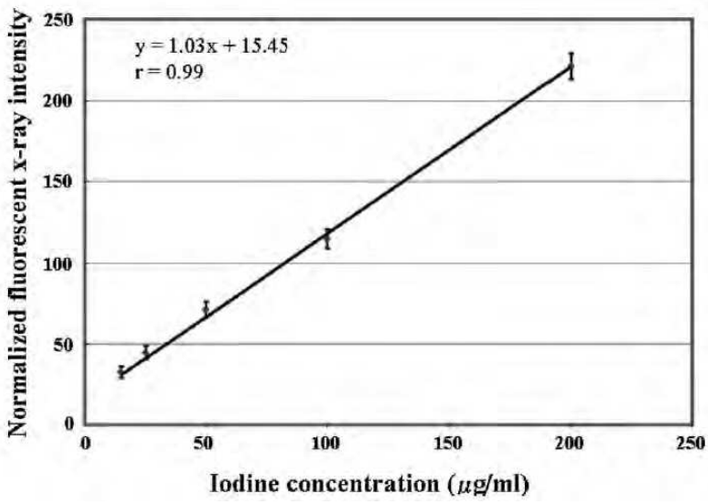

Fig. 12. Relationship between actual iodine concentration and FXCT pixel value.

3.4.2 Ex Vivo imaging of hamster's heart

With FXCT using synchrotron radiation, we successfully imaged the myocardial fatty acid metabolism in normal rat and cardiomyopathic hamster with BMIPP (^{127}I-BMIPP) labelled with non-radioactive iodine, where the BMIPP is a potential tracer for detecting the fatty acid metabolism in current clinical SPECT imaging (Thet-Thet-Lwin, et al., 2007; —, 2008). In this study the myocardial fatty acid metabolism in cardiomyopathic hamster and age-matched normal hamster were quantitatively analyzed using FXCT images, and the FXCT images were compared with optical microscope images with Masson's trichrome (MT) stain.

A 20 week J2N-k cardiomyopathic hamster and an age matched J2N-n normal hamster were imaged in this study. Under anesthesia (pentobarbital 40 mg kg^{-1} weight), hearts were extracted after 5 min intravenous injection of ^{127}I-BMIPP (0.08 mg g^{-1} weight). The hearts labeled with BMIPP were fixed by formalin and then imaged by FXCT, placing them in an acrylic cell under the same data acquisition parameters as for the phantom study. Here, five short-axis slices of heart in cardiomyopathy and three short-axis slices in normal hamster were imaged by FXCT. After FXCT imaging, specimens were cut into 0.02 mm thick slices. The degree of fibrosis and its area were evaluated by optical microscopy (Biozero, Keyence Co., Japan) with MT stain, because fibrotic tissue does not uptake BMIPP.

FXCT images revealed that BMIPP was distributed homogeneously in normal myocardium, whereas it was distributed heterogeneously in cardiomyopathic myocardium. In normal hamster, the mean BMIPP uptake value of each slice was not statistically different among the three short-axis images: 177.2 ± 18.5, 180.1 ± 17.9 and 179.1 ± 18.0. In cardiomyopathic hamster, the mean BMIPP uptake value of each slice was also not statistically significant among the five short-axis images: 151.1 ± 26.5, 164.6 ± 25.8, 157.8 ± 23.1, 150.0 ± 24.7 and 149.0 ± 25.6. The mean BMIPP uptake value of each slice in cardiomyopathic hamster heart was lower than that in normal heart and its standard deviation was larger than that of normal heart. Short-axis images of the mid-ventricular level in normal and cardiomyopathic hamsters (Figs. 13 (a) and (b)) were analyzed in detail for regions of each slice. In these images the mean BMIPP uptake in normal myocardium was 1.2 times higher than that in cardiomyopathic myocardium (177.2 ± 18.5 mg ml^{-1} versus 151.1 ± 26.5 mg ml^{-1}). In the same slices as used for the FXCT image, optical microscopy with MT stain depicted no fibrosis in normal myocardium and only a slight interstitial fibrosis in cardiomyopathic myocardium (Figs. 13 (c) and (d)). An area of 12.0% was observed as interstitial fibrosis in the whole short-axis slice of the mid-left ventricle. Areas of this interstitial fibrosis partially corresponded to that of reduced BMIPP uptake in the FXCT images (Table 1). In addition, morphological structures such as papillary muscle, wall thickness and left ventricle diameter were also approximately visualized in the FXCT images. Ventricular dilatation and mild thinning of the myocardial wall were observed in the cardiomyopathic myocardium cases.

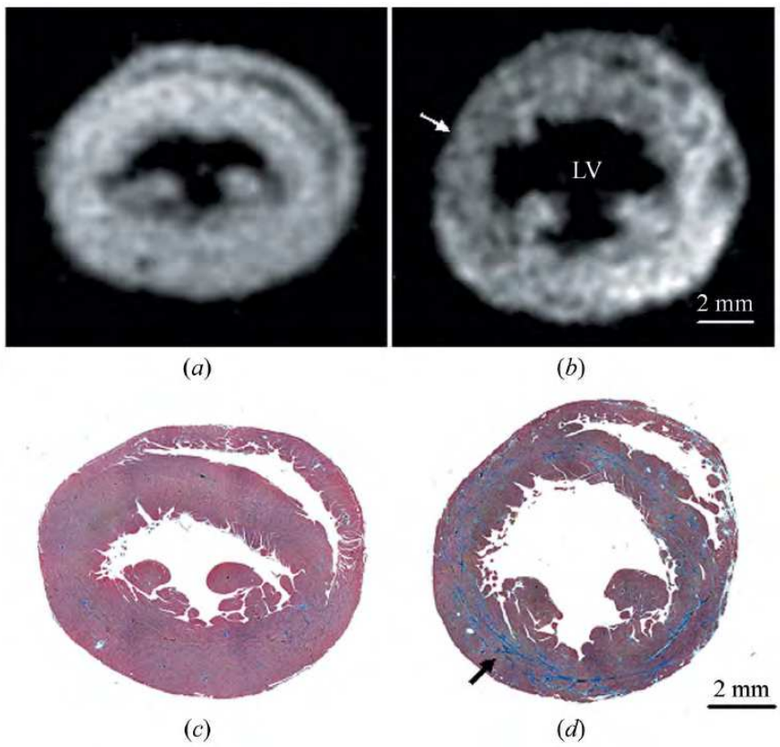

Fig. 13. FXCT images of (a) normal myocardium and (b) cardiomyphathic myocardium. Optical microscope pictures with MT stain of (c) normal and (d) cardiomyopathic myocardium (Thet-Thet-Lwin, et al., 2007; —, 2008).

State	Left-ventricle regions			
	Anterior wall	Lateral wall	Inferior wall	Septum
Normal (μg ml^{-1})	176.3 ± 13.4	174.3 ± 12.5	179.2 ± 15.2	181.1 ± 14.3
Cardiomyopathy (μg ml^{-1})	167.5 ± 24.1	156.8 ± 22.7	134.5 ± 19.5	147.1 ± 28.2
Uptake − 2SD of normal myocardium (%)	18.3	20.7	75.5	41.3
Percentile fibrosis area (%)	6.9	15.3	11.5	12.3

Table 1. Mean BMIPP uptake, and percentile area of reduced BMIPP uptake and fibrosis for each myocardinal region of the mid-left ventricle (Thet-Thet-Lwin, et al., 2007; —, 2008).

3.4.3 Ex Vivo and In Vivo imaging of mouse's brain

Using x-ray fluorescent computed tomography (FXCT), the in vivo and ex vivo cerebral distribution of a stable-iodine-labeled cerebral perfusion agent, iodoamphetamine analog (^{127}I-IMP), has been recorded in the brains of mice (Takeda et al., 2009). In vivo cerebral perfusion in the cortex, hippocampus and thalamus was depicted at 0.5 mm in-plane spatial resolution. Ex vivo FXCT images at 0.25 mm in-plane spatial resolution allowed the visualization of the detailed structures of these regions. The quality of the FXCT image of the hippocampus was comparable with the ^{125}I-IMP autoradiogram. These results highlight the sensitivity of FXCT and its considerable potential to evaluate cerebral perfusion in small animals without using radioactive agents.

We obtained images from seven living mice, weighing 20–24 g with heads of diameter about 20 mm, after we employed a 10 mm-diameter contrast-resolution acrylic phantom to assess the contrast resolution in an ex vivo brain. The phantom consisted of three 5 mm-diameter axial cylindrical channels filled with three different iodine solutions, their concentrations ranging from 0.005 to 0.1 mg ml^{-1}. We used non-radioactive ^{127}I-labeled N-isopropyl-p-iodoamphetamine (^{127}I-IMP containing 0.38 mg iodine) for in vivo imaging of the brain, while radioactive ^{123}I-IMP is commonly employed to evaluate cerebral perfusion in clinical SPECT studies. Imaging started 5 min after intravenously injecting ^{127}I-IMP into a mouse anesthetized with pentobarbital; this dose is similar to that used by others in animal SPECT studies. The head of the mouse was set in the vertical direction to the pencil beam, fixed by an animal head holder to suppress any movement. Since the amount of IMP in the brain declined gradually with the approximate half-life time of 1.5 h, we surgically removed the *brain* of another mouse for the ex vivo experiments 5 min after intravenously injecting the ^{127}I-IMP and fixed it in the formalin. Then it was set within a formalin-filled acrylic cell, and imaged by FXCT at 0.5 mm and 0.25 mm in-plane spatial resolution. The FXCT image of the phantom was obtained at 0.25 mm in-plane spatial resolution. For comparison, we obtained autoradiograms with radioactive ^{125}I-IMP from two other mice. Their brains were removed surgically 5 min after injecting ^{125}I-IMP (15 kBq kg^{-1}), fixed in formalin, and cut into 0.02 mm slices. These samples were exposed on an imaging plate (IP) for 48 h, and the plate was read by a BAS 5000 (Fuji) IP reader at 0.05 mm scan steps and 16-bit depths.

The in vivo FXCT image at a 0.5 mm in-plane spatial resolution revealed the cerebral perfusion of ^{127}I-IMP throughout the brain of the mouse (Fig. 14), whereas absorption-contrast x-ray transmission CT (XTCT) discriminated only between the soft tissue and the bony structures of the skull. Cerebral perfusion in the cortex and hippocampus was more

clearly visualized in the 0.5 mm in-plane spatial resolution FXCT image than in the 1 mm in-plane resolution image, while the anatomical features of the skull bone were clearly demonstrated by XTCT. Furthermore, the superimposed image (FXCT and XTCT) demonstrated the correspondence between anatomical features and cerebral perfusion (Zeniya, et al., 2001). The measured SNR of the FXCT image in cerebral cortex, hippocampus and thalamus was about 12.3, 11.7 and 21.1, respectively. We calculated that the mouse experienced a radiation-absorbed dose of about 0.36 Gy for the FXCT imaging experiment.

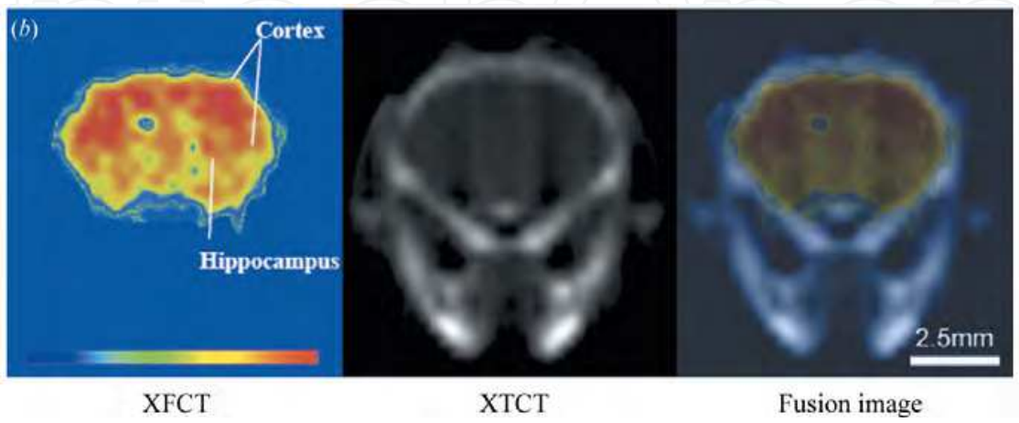

Fig. 14. In vivo FXCT, TCT and superimposed images of normal mouse brains obtained at 0.5 mm in-plane spatial resolution (Takeda et al., 2009).

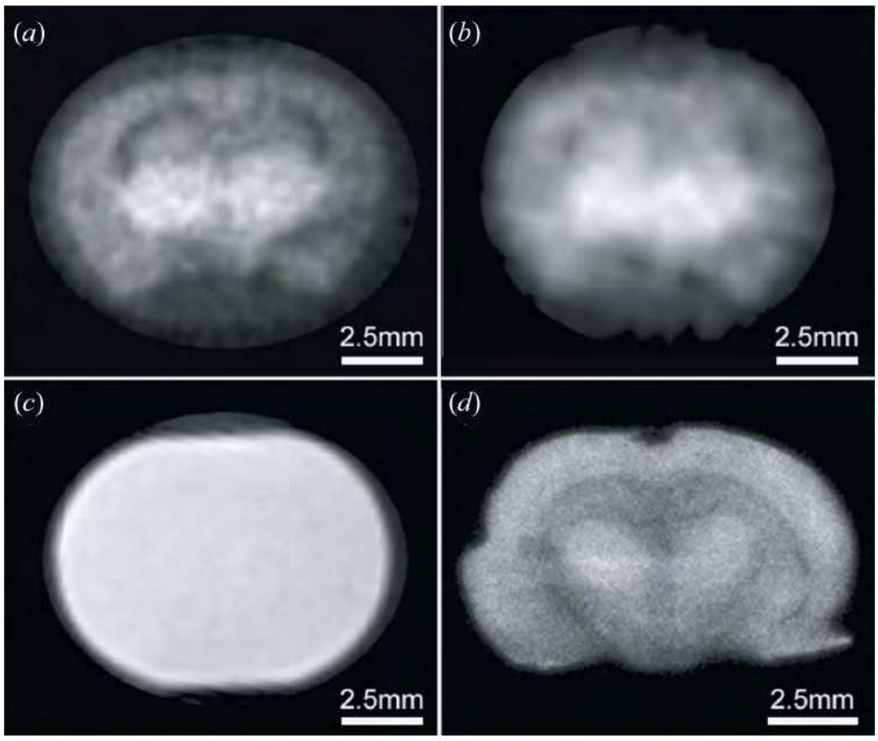

Fig. 15. FXCT image of formalin-fixed (ex vivo) mouse brain set within an acrylic cell filled with formalin (a, b, c), and autoradiogram with ^{125}I-IMP (d) (Takeda et al., 2009).

FXCT clearly imaged the formalin-fixed brain in an acrylic cell both at a 0.5 mm and a 0.25 mm in-plane spatial resolution, while, in contrast, the XTCT image discriminated only the margin of the acrylic cell, and failed to distinguish the rain from its surrounding solution (Fig. 15). An ex vivo FXCT image was obtained in the same slice level; however, the FXCT image at 0.25 mm in-plane spatial resolution clearly differentiated the detailed structures, such as the cortex, hippocampus and thalamus, with almost the same quality as an autoradiogram with radioactive ^{125}I-IMP. The IMP dose was approximately 27.3, 23.8 and 50.3 mg g^{-1} in the cortical surface, hippocampus and thalamus, respectively.

4. SR-FXCT based on sheet beam geometry

As for *in vivo* imaging, FXCT has a problem: the conventional FXCT takes a huge amount of measurement time to acquire a single tomographic image because it adopts the sequential data collection scheme with a pencil beam, which is the first generation of data acquisition scheme in CT. Although it is desirable to collect as much data as possible for a high-quality image, the whole measurement must be completed under anesthesia and then the number of data points is severely restricted. Therefore, we have not yet attained the potential spatial resolution for *in vivo* imaging.

4.1 SR-FXCT imaging system with sheet beam geometry

The long measurement time of conventional FXCT based on pencil beam geometry is due to sequential data acquisition, and for faster measurements simultaneous or parallel acquisition of a single projection is indispensable. Figure 16 shows a schematic diagram of the proposed imaging geometry (Huo, et al., 2008; —, 2009). An incident monochromatic sheet beam, where the photon fluxes are parallel to one another, impinges on the object as it covers the width of the object cross section. Contrast agents, such as iodine, are thus excited and then isotropically emit x-ray fluorescence photons on de-excitation. A linear array of detectors, where N solid-state detectors operating in a photon counting mode with energy resolution are equally spaced, is positioned perpendicular to the beam propagation in the plane of polarization for the lowest Compton scatter contribution in the spectrum, due to the property of linear polarization. A long slit-like collimator is installed in front of each

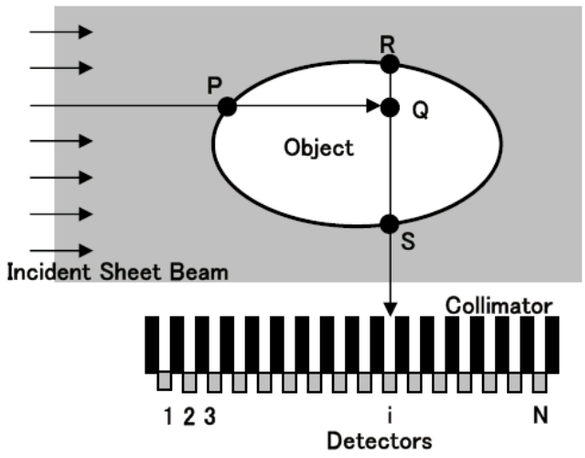

Fig. 16. FXCT based on sheet-beam geometry (Huo, et al., 2008).

detector element in order to restrict the regions emitting x-ray fluorescence incident on the detector surface and to reduce the amount of stray radiation being detected. As a result, the detector array from the 1st to the *N*th detectors simultaneously acquires projection data in a direction perpendicular to the beam propagation. Translational scans are therefore no longer required during the collection of a set of projections, though some translational scans may still be necessary to obtain a single complete projection, because each detector is partitioned by a collimator and no data are obtained at the collimator's septal walls. The overall measurement time will still be drastically reduced, as a set of projections can be collected through rotational and fewer translational scans.

4.2 Formulation and reconstruction

We set the x_1x_2-coordinate fixed to the object, and suppose that the sheet beam accompanied with the detectors array is rotated around the origin O, where the collimators in front of the array are omitted so as to see easily the diagram. The hatched region means the incident sheet-beam irradiation. We derive the formula representing fluorescent x-ray photons measured by a single detector, or the *i*th detector among *N* detectors of the array. First, we pay attention to a single incident ray among the sheet beam. The points, P, Q, S and R in Fig. 17 represent the intersection of the single incident ray with the object's surface, the point of interest, an intersection of a single emitted fluorescent x ray with the object's surface, and an intersection of line QS with the object's surface, respectively. We denote the iodine concentration distribution to be estimated, the distribution of the linear attenuation coefficient for the energy of the incident X-ray, and that of the fluorescent X-ray as $d(x)$, $a_I(x)$ and $a_F(x)$ must be known in advance by the usual x-ray CT using the CCD camera. Next, let us consider the process in which a single incident ray with an initial intensity I_0, at the point, P, arrives at the point, Q, and the fluorescent subsequently emitted x ray from the iodine atoms excited at the point, Q, reaches the *i*th detector. We partitioned the process into three steps. Here, $\theta \in S^1$ and $\theta^{\perp} \in S^1$ are unit vectors parallel and vertical to the single ray of interest.

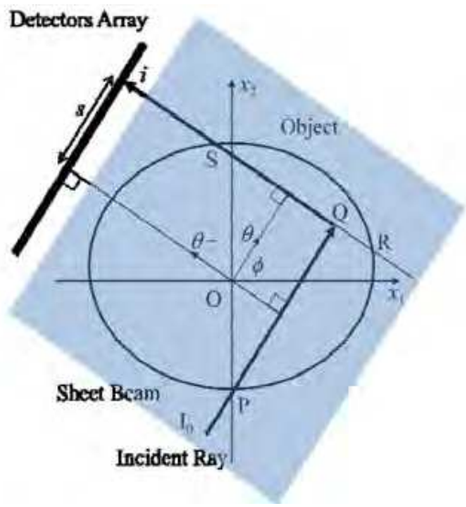

Fig. 17. Sheet-beam based FXCT geometry

Step 1: The x-ray flux rate, $I(x)$, reaching the point, Q, is given by

$$I(x) = I_0 \exp\left[-(Da_I)(x,\theta)\right] \tag{18}$$

where

$$(Da_I)(x,\theta) = \int_0^\infty a_I(x - t\theta)dt \ .$$

Step 2: The fluorescent x-ray is emitted isotropically with an intensity proportional to the product of the absorbed x-ray flux rate at the point, Q, $\mu_{ph}\ I(x)\ \Delta v$ and the iodine concentration, $d(x)$, where μ_{ph} is the photoelectric linear attenuation coefficient of iodine, and Δv is the differential volume at Q. Accordingly, the flux rate of the fluorescent x ray emitted from the point, Q, and reaching the ith detector, $f(x)$, is given by

$$f(x) = I(x)d(x)\mu_{ph}\omega\Delta v\, \Omega/4\pi \tag{19}$$

where ω and Ω are the yield of the fluorescent x ray and the solid angle at which the point, Q, is viewed by the ith detector, respectively.

Step 3: Following a fluorescent x-ray emitted from the point, Q, crossing the object toward the ith detector, it is attenuated along the line segment QS; it reaches the ith detector with a flux rate given by

$$I_d(x) = \exp\left[-(Da_F)(x,\theta^\perp)\right] f(x) \tag{20}$$

where

$$(Da_F)(x,\theta^\perp) = \int_0^\infty a_F(x + t\theta^\perp)dt \ .$$

Here, we obtained the contribution from the single incident ray into the ith detector. The formula holds for other rays among the sheet beam. The total flux rate of the fluorescent x-ray reaching the ith detector for the sheet beam x-ray is obtained by integrating with respect to x along line RS, $x \bullet \theta = s$, where s is a distance between origin O and line RS:

$$\left(R_a f\right)(\theta,s) = \int_{x\theta=s} \exp\left[-(Da_F)(x,\theta^\perp)\right] f(x)\, dx \tag{21}$$

Thus, the measurement process by the FXCT based on sheet beam geometry leads to the attenuated Radon transform. The inversion for $g = R_a f$ was given by Natterer (Natterer, 2001) as

$$f(x) = \frac{1}{4\pi}\mathrm{Re}\ div \int_{S^1} \theta \exp\left[-(Da_F)(x,\theta^\perp)\right]\left(e^{-h}He^{h}g\right)(\theta, x\theta)\, d\theta \tag{22}$$

where $h = 1/2(I + iH)Ra_F$, and H and R are the Hilbert transform and Radon transform, respectively. We can obtain the exact iodine density $d(x)$ by first applying the exact inversion formula straightforwardly to Eq. (22), and then by applying Eq. (19) to the resulting $f(x)$. In the sheet-beam geometry, the analytical solution is exactly feasible.

4.3 Preliminary experiments

In order to prove the concept of this imaging protocol, we constructed a preliminary imaging system for simulating the proposed imaging geometry using a single HPGe SSD.

4.3.1 Imaging setup

The preliminary imaging system was constructed at the BLNE-5A bending-magnet beam line (6.5 GeV), KEK in Japan. A white x-ray beam from a source was monochromatized using a Si (220) monochromator at 37 keV. The photon flux rate in front of the object was approximately 9.3×10^7 photons/mm²/s for a beam current of 40 mA. The monochromatized beam was shaped to a sheet beam of 2.0 cm wide × 1.0 mm thick using an x-ray slit. Figure 18 shows the schematic of the preliminary detection system for simulating a sheet-beam geometry, consisting of an HPGe detector operating in photon counting mode to detect emitted fluorescent photons and a long Pb slit collimator installed in front of the detector surface. We prepared two types of collimators: one coarse (1.0 mm height × 0.5 mm width × 100 mm long) and the other fine (1.0 mm height × 0.25 mm width × 100 mm long). The distance between the sample surface and the collimator tip was set at 12 mm. First the sample was scanned translationally along the beam direction and, after the translational scan, the sample was rotated. Although the data collection scheme is sequential, the dataset finally obtained corresponds to that acquired using a linear array of detectors. Projection data at the data point was generated from the K_α peak by summing the fluorescent-photon counts in the energy window with the center at 28.3 keV and width of 2 keV.

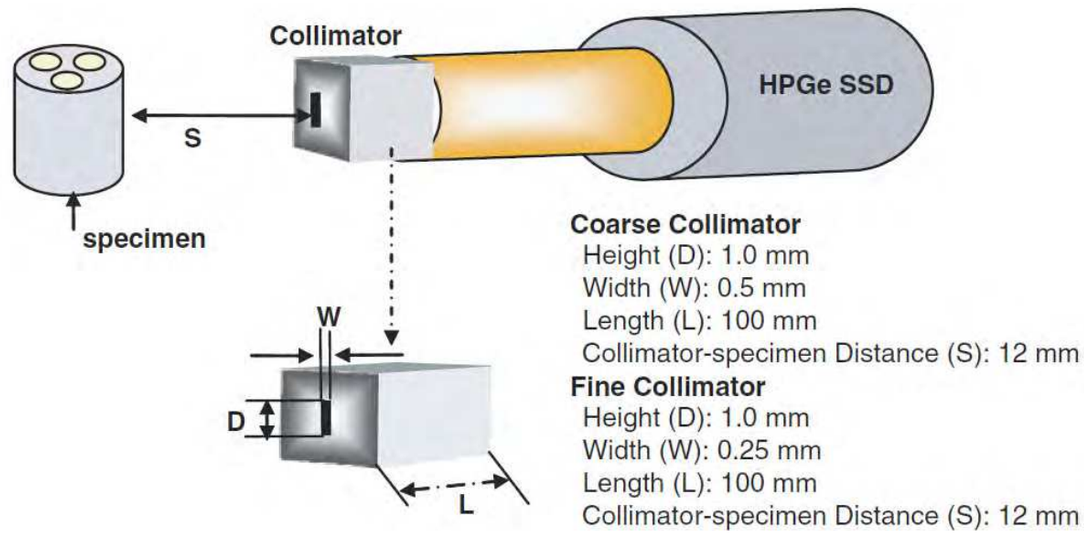

Fig. 18. Schematic of a lead collimator and a solid state detector.

4.3.2 Phantom imaging

To confirm the efficacy, we performed an imaging experiment using a physical phantom, which is a 10-mm-diameter acrylic cylinder with three 3-mm-diameter holes filled with iodine solutions at different concentrations (200, 100, and 50 μg/ml). The sample was imaged twice. First, it was scanned using the coarse collimator translationally and rotationally at 0.5-mm steps and 2° steps over 180°, respectively. The measurement time for

a data point was 5 s, and dead-time rate was less than 10%. Second, it was done using the fine collimator translationally and rotationally at 0.25-mm steps and 2° step over 180°, respectively. The measurement time for a data point was 5 s and dead-time rate was less than 5%. The reconstructed images for the coarse and fine collimators are shown in Figs. 19 (a) and (b), respectively. In both the images, the three circles corresponding to the regions including the iodine solution are successfully delineated, but the image for the coarse collimator is more blurred than that for the fine collimator. Figure 19 suggests that pixel values in the iodine regions depend on the actual iodine concentration. So, we investigated the imaging scheme quantitatively using the physical phantom. For this, we imaged the phantom while changing the iodine concentrations, and then compared the actual iodine concentrations with the average pixel values in the iodine regions set in the reconstructed images. Figure 20 shows the relationship. A good correlation was observed between the pixel value in the reconstructed image and the iodine concentration (R = 0.99). We can use the result as the calibration line for quantitative measurement.

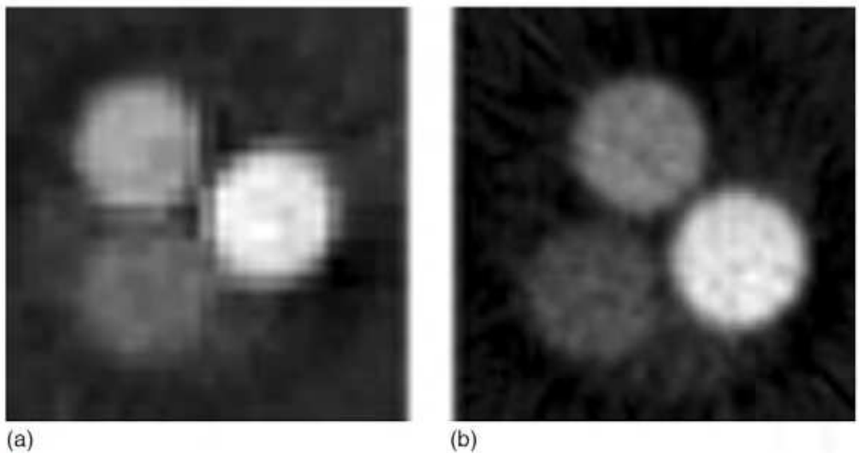

Fig. 19. FXCT image of a 10-mm-diameter acrylic cylindrical phantom which has three channels (3 mmϕ) filled with three different concentrations of iodine solution: (a) coarse collimator, (b) fine collimator (Huo, et al., 2009).

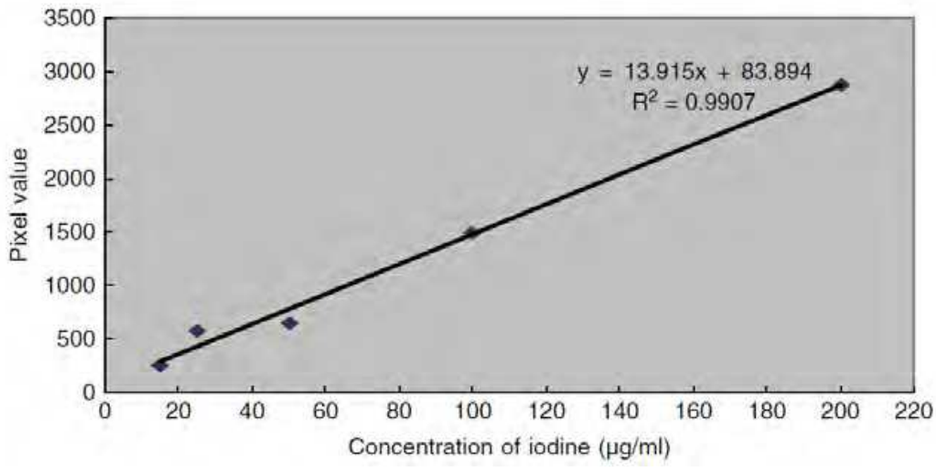

Fig. 20. Relationship between actual iodine concentration and FXCT pixel value.

4.3.3 Ex Vivo imaging of mouse's brain

We imaged a normal mouse brain *ex vivo* in order to confirm the suitability of the technique for biomedical imaging. Under anesthesia, the brain of a mouse was extracted after 5 min intravenous injection of non-radioactive iodine labeled ^{127}I-IMP (about 0.05 mg/ml) and fixed by formalin. This experiment was approved by the Medical Committee for the Use of Animals in Research of the University of Tsukuba, Japan. The brain was fixed in an acrylic cylinder filled with formalin and was put on the stage (Fig. 21). The sample was imaged twice. First, it was scanned using the coarse collimator translationally and rotationally at 0.5-mm steps and 2° step over 180°, respectively. The measurement time for a data point was 20 s and dead-time rate was less than 10%. Second, it was done using the fine collimator translationally and rotationally at 0.25-mm steps and 2° step over 180°, respectively. The measurement time for a data point was 20 s and dead-time rate was less than 5%. The reconstructed images for the coarse and fine collimators are shown in Figs. 22 (a) and (b), respectively. The reconstructed image for the coarse collimator is more blurred than that for the fine collimator. However, in the both images, the cortex and thalamus can be identified anatomically, and the iodine content of the brain is estimated to be about 20.0 μg/ml on average using the calibration line in Fig. 20. The iodine content approximately coincides with that obtained using the system based on a pencil-beam geometry. From these results we can conclude that the proposed scheme can also offer quantitative biomedical information related to cerebral perfusion at a high spatial resolution.

Fig. 21. Extracted mouse brain put in an acrylic cylinder filled with formalin.

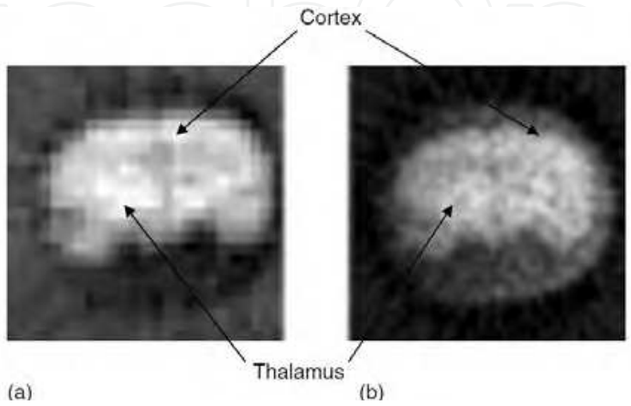

Fig. 22. Ex vivo FXCT images of normal mouse brain: (a) coarse collimator, and (b) fine collimator (Huo, et al., 2009).

5. Considerations

Here, we investigate the differences between FXCTs based on pencil-beam and sheet-beam geometries in their imaging properties by considering each measurement process in detail. As shown in Fig. 23 (a), in the pencil-beam geometry a thin incident beam impinges on an object and excites imaging agents on the incident beam line, and then fluorescent x-ray photons are isotropically emitted from the imaging agents. Pay attention to the point Q inside the object in order to consider the measurement process in a more detail. The measurement process is broadly divided into three steps in the following:

A. The incident flux travels from P to Q while being attenuated by the object.
B. The fluorescent flux of X-ray photons is isotropically emitted at Q in proportion to the product of the incident intensity and the concentration of imaging agents at Q. Of the photons, only those that propagate toward the detective surface ST are detected.
C. The fluorescent flux travels from Q to the detector surface ST while being attenuated by the object. Here, the amount of attenuation depends on the propagation direction. For example, while the fluorescent flux reaching points W and X on the detector surface ST is attenuated by segments QU and QV, respectively, the amount of attenuation is different.

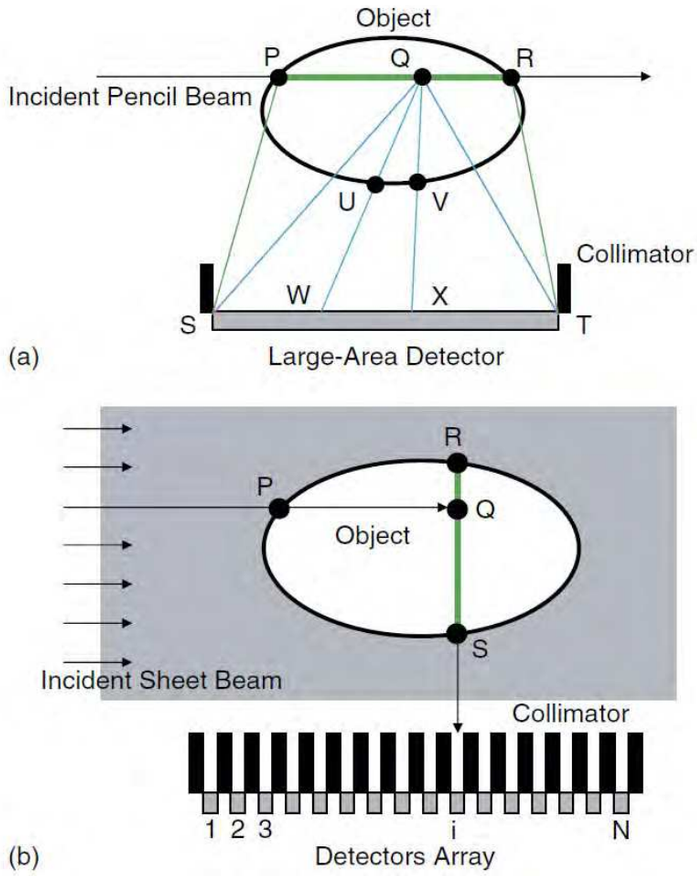

Fig. 23. Schematics of measurement process: (a) pencil-beam geometry, and (b) sheet-beam geometry.

Since the fluorescent flux obtained above is a contribution from the point Q, the total detected photons can be obtained by integration through PR. The measurement process of the pencil beam geometry is very complex, and hence the attenuation correction also is very complex. In sheet-beam geometry, concerning the measurement by the *i*th detector along path P→Q→S in Fig. 23 (b), the measurement process is divided into three steps:

A. The incident flux is attenuated by an object during the propagation from points P to Q.
B. The x-ray fluorescence photons are isotropically emitted at point Q, whose number is proportional to both the incident flux rate and the iodine quantity at point Q.
C. The fluorescent flux travels toward the detector while being attenuated by the object during the propagation from point Q to S.

As each point on line RS is similarly subjected to the above process, the number of fluorescent photons detected by the *i*th detector is obtained by integrating the contributions from all the points on RS. The measurement process of the sheet-beam geometry is very simple, and therefore the attenuation correction is relatively simple.

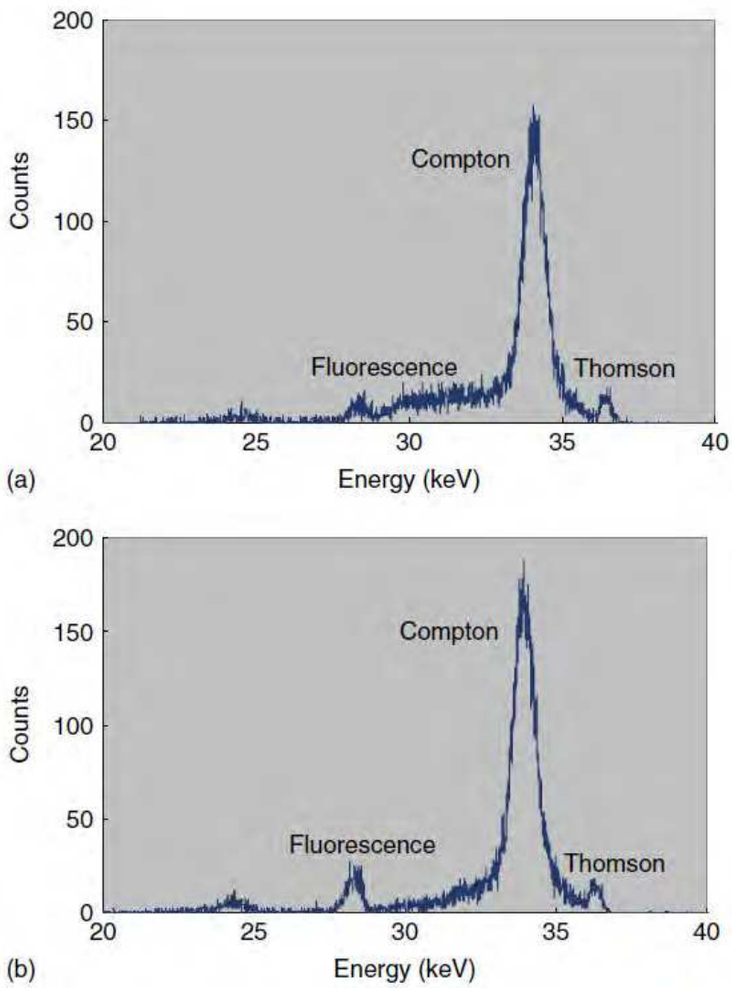

Fig. 24. Example of energy profile: (a) pencil-beam geometry, and (b) sheet-beam geometry (Huo, et al., 2009).

First, we consider signal quality based on the above specification on the measurement process. Figures 24 (a) and (b) show the energy profile obtained from the identical physical phantom using the systems based on pencil- and sheet-beam geometry, respectively. In both the figures, fluorescence, Compton scatter, and Thomson scatter peaks are observed from the left to the right. The first point to notice is that the counts in a region between the fluorescent and the Compton peaks, which correspond to multiple scatter components, in the pencil-beam geometry is more than those in the sheet-beam geometry, although the energy profiles are very similar in appearance. In the pencil-beam geometry, the detector collects a great deal of multiply scattered components from various directions because of the use of a large area of the detector surface. On the other hand, in the sheet-beam geometry, the detection efficiency of fluorescence is remarkably low because of the use of the slit-like collimator. However, the collimator in turn suppresses the scattered components maximally. Therefore, the system based on sheet-beam geometry can measure fluorescence under less dead-time ratio of the detector, and thus it can collect data more reliably than the system based on pencil-beam geometry.

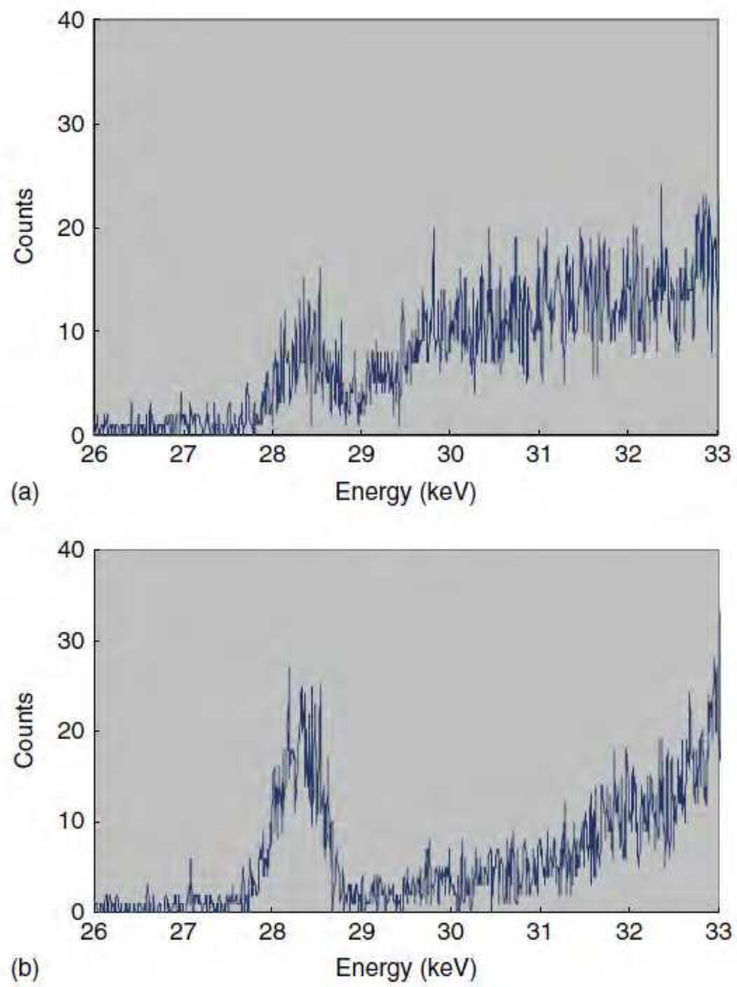

Fig. 25. Example of energy profile around the fluorescent peak: (a) pencil-beam geometry, and (b) sheet-beam geometry (Huo, et al., 2009).

Figures 25 (a) and (b) show the enlarged energy profiles around the fluorescent peaks for the pencil- and sheet-beam geometry, respectively, where Figs. 25 (a) and (b) are respectively generated from Figs 24 (a) and (b). From Fig. 25 (a), in the pencil-beam geometry, we can see that the multiply scattered components overlap with the fluorescent peak. In contrast, the background noise in the fluorescence region is not observed in Fig. 25 (b). Therefore, we can conclude that the system based on the sheet beam geometry can detect data at a higher signal-to-noise ratio than that on the pencil-beam geometry. The higher quantitative results described earlier can be attributed to the above factors.

Next, we consider a relationship between the spatial resolution and the measurement time. In the sheet-beam geometry, the spatial resolution of the reconstructed image mainly depends on the slit width of the collimator installed in front of the detector, as discussed earlier. In principle, the measurement time depends less on the resolution, because a single projection is obtained simultaneously or in parallel. On the other hand, in the pencil beam geometry, the resolution depends on the cross section of the thin incident beam. Reduction of the beam cross section for higher resolution leads to reduction of the translational step, and therefore the measurement time to acquire a single projection increases. Therefore, the sheet-beam geometry is indispensable for compatibility of the measurement time with the resolution.

Finally, we estimate the measurement time. Using an array of 100 energy-resolved detectors, each with a detector surface 0.25 mm in width and arrayed equally 0.25 mm apart, three translations at steps of 0.25 mm can produce a single complete projection of 25 mm in width. On the assumption that the time for a single measurement is 5 s and the rotational step is 2° over 180°, the total time is 900 (= 5 × 2 × 90) s, plus the time required for the mechanical scans. Thus, we can image a single object in about 15 min. If the detector elements are two-dimensionally arrayed, we can obtain a 3-D CT image by piling up the 2-D tomographic images.

6. Conclusion

In this chapter, we first introduced FXCT of the first generation based on pencil-beam, which offers excellent imaging properties, such as high spatial resolution, high sensitivity, and high quantitativeness. Especially, spatial resolution can be improved up to the microns range by decreasing cross-section of incident-beam. However, the measurement time increases because a decrease in beam cross-section causes a reduction of step size in translationally scanning incident beam, leading to an increase in the number of data, and further an increase in the measurement time. Therefore, in FXCT based on pencil-beam the measurement time and the spatial resolution have a trade-off relationship, since it collects data sequentially. Long measurement time is fatal to in vivo imaging, i.e., molecular imaging.

Then, in order to circumvent the above problem, we proposed the parallel data-acquisition scheme based on sheet-beam geometry. This method collects a set of data in a single projection at once, and thus drastically reduces the total measurement time. We experimentally proved the feasibility by demonstrating reconstructed images of a physical phantom and a biomedical sample using a preliminary system constructed at KEK, Japan.

The proposed method based on sheet-beam geometry also preserves the excellent imaging properties. Also, we take notice of the fact that the sheet-beam geometry offers the exact analytical solution. In addition, the FXCT system can acquire not only functional information but also morphological one. If the CCD camera is placed downstream of the object, we can simultaneously obtain a transmission image which can provide auxiliary data for attenuation correction and morphological information. The proposed FXCT can, therefore, simultaneously obtain both morphological and functional information, while PET/CT requires separate measurements to obtain the two kinds of images.

7. A view to the future

The problem left is how to reconstruct 3-D image. PET and SPECT produce 3-D images. If FXCT gives only 2-D images in spite of a good spatial resolution, FXCT ranks with PET and SPECT. However, the problem can be solved using 2-D detectors array and a volumetric parallel incident beam. If we treat the volumetric beam as an accumulation of sheet beams in a vertical direction, we can apply the proposed data-acquisition scheme and the reconstruction algorithm to each supposed sheet-beam straightforwardly. Finally, we construct a 3-D image by accumulating the reconstructed 2-D images in a vertical direction. The measurement time in 3-D case is the same as that in 2-D case. For this purpose, we need a 2-D detectors array with energy resolution. However, presently it is still too expensive, and has an insufficient size of each detector element. Advent of 2-D detectors array with energy resolution and with each detective surface area sufficiently fine will accelerate development of the FXCT system for molecular imaging.

8. Take-home-message

FXCT is a hybrid from x-ray fluorescent analysis and computed tomography. FXCT imaging system has excellent properties as follows:

1. use of non-radioactive imaging agent, i.e., non-inner exposure inspection,
2. non-destructive measurement,
3. high sensitivity,
4. high spatial resolution,
5. high quanatitativeness, and
6. simultaneous acquisition of functional and morphological information.

9. Acknowledgment

We would like to thank Professor Emeritus Takao Akatsuka (Yamagata University) for adequate advice through the research for long years. Also, we thank Kazuyuki Hyodo PhD, Thet-Thet-Lwin MD, Jin Wu MD, Qingkai Huo PhD, Naoki Sunaguchi PhD, Quanwen Yu PhD, Masahiro Akiba PhD, and Tsutomu Zeniya PhD for their scientific and technical supports. This research was partially supported by a Grant-In-Aid for Scientific Research (No. 21390339 & 23602002) from the Japanese Ministry of Education, Science and Culture, and performed under the auspices of the National Laboratory for High Energy Physics (2010G055).

10. References

Boisseau, P. & Grodzins, L. (1987), Fluorescence tomography using synchrotron radiation. Hyperfine Interactions, Vol. 33, pp. 283–292

Brunetti, A. & Golosio, B. (2001). Software for X-ray fluorescence and scattering tomographic reconstruction. *Computer Physics Communications*. Vol. 141, No. 3, pp. 412-425

Cesareo, R. & Mascarenhas, S. (1989). A new tomographic device based on the detection of fluorescent X-rays. Nucl. Instrum. Mech., Vol. A277, pp. 669–672

Cheong, S. K.; Jones, B. L.; Siddiqi, A. K.; Liu, F; Manohar, N & Cho, S. H. (2010). X-ray fluorescence computed tomography (XFCT) imaging of gold nanoparticle-loaded objects using 110 kVp x-rays. *Physics in Medicine and Biology*, Vol. 55, Iss. 3, pp. 647-662

Chukalina, M.; Simionovici, A; Snigirev, A. & Jeffries, T (2002). Quantitative characterization of microsamples by x-ray fluorescence tomography. *X-Ray Spectrometry*, Vol. 31, Iss. 6, pp. 448-450

Chukalina, M.; Simionovici, A.; Zaitsev, S. & Vanegas, C. J. (2007). Quantitative comparison of X-ray fluorescence microtomography setups: Standard and confocal collimator apparatus. *Spectrochimica ACTA Part B - Atomic Spectroscopy*, Vol. 62, Iss. 6-7, pp. 544-548

Deng, B. A.; Yang, Q.; Xie, H. L. .; Du, G. H. & Xiao, T. Q. (2011). First X-ray fluorescence CT experimental results at the SSRF X-ray imaging beamline. *Chinese Physics C*, Vol. 35, Iss. 4, pp. 402-404

Deng, B; Yu, X. H.; Li, A. G.& Xu, H. J (2007). Nondestructive analysis by combined X-ray tomography on a synchrotron radiation facility. *Nuclear Science and Techniques*, Vol. 18, Iss. 5, pp. 257-260

Golosio, B.; Simionovici, A.; Somogyi, A.; Lemelle, L.; Chukalina, L. M. & Brunetti, A. (2003). Internal elemental microanalysis combining x-ray fluorescence, Compton and transmission tomography. *J. Appl. Phys*., Vol. 94, No. 1, pp. 145-156

Golosio, B.; Simionovici, A.; Somogyi. A; Camerani, C. & Steenari, B. M. (2003). X-ray fluorescence tomography of individual waste fly ash particles. *Journal de Physique IV*, Vol. 104, pp. 647-650

Hogan, J. P.; Gonsalves, R. A. & Krieger, A. S. (1991). Fluorescent computer tomography: A model for correction of X-ray absorption. *IEEE Trans. Nuc. Sci.*, Vol. 38, pp. 1721–1727

Huo, Q.; Yuasa, T.; Akatsuka, T.; Takeda, T.; . Wu, J.; Thet-Thet-Lwin; Hyodo, K. & Dilmanian, F. A. (2008). Sheet beam geometry for in vivo fluorescent x-ray computed tomography : Proof-of-concept experiment in molecular imaging. *Opt. Lett.*, Vol. 33, Iss. 21, pp. 2494-2649

Huo, Q.; Sato, H.; Yuasa, T.; Akatsuka, T.; Wu, J.; Thet-Thet-Lwin; Takeda, T. & Hyodo, K. (2009). First experimental result with fluorescent X-ray CT based on sheet-beam geometry. *X-Ray Spectrometry*, Vol. 38, pp. 429-445

Iida, A & Gohshi, Y. (1991). Tracer element analysis by X-ray fluorescent, In: *Handbook on Synchrotron Radiation*, vol. 4, S. Ebashi, M. Koch, and E. Rubensein, (Eds.), 307–348, , North-Holland: Elsevier, Amsterdam, Netherlands

Jones, B. L. & Cho, S. H. (2011). The feasibility of polychromatic cone-beam x-ray fluorescence computed tomography (XFCT) imaging of gold nanoparticle-loaded objects: a Monte Carlo study. *Physics in Medicine and Biology*, Vol. 56, pp. 3719-3730

La Riviere, P. J. (2004). Approximate analytic reconstruction in x-ray fluorescence computed tomography. *Physics in Medicine and Biology*, Vol. 49, pp. 2391-2405

La Riviere, P. J. & Vargas, P. A. (2006). Monotonic penalized-likelihood image reconstruction for X-ray fluorescence computed tomography. *IEEE Trans. Med. Imaging*, Vol. 25, Iss. 9, pp. 1117-1129

La Riviere, P. J.; Billmire, D; Vargas, P; Ri ers, M & Sutton, S. R. (2006). Penalized-likelihood image reconstruction for x-ray fluorescence computed tomography. *Optical Engineering*, Vo. 45, Iss. 7, 077005

La Riviere, P.; Vargas, P.; Xia, D. & Pan, X. C (2010). Region of Interest Reconstruction in X-Ray Fluorescence Computed Tomography for Negligible Attenuation. *IEEE Trans. Nuclear Science*, Vol. 57, Iss. 1, pp. 234-241

Miqueles, E. X. & De Pierro, A. R. (2010). Exact analytic reconstruction in x-ray fluorescence CT and approximated versions. *Physics in Medicine and Biology*, Vol. 55, No. 4, pp. 1007-1024

Miqueles, E. X. & De Pierro, A. R. (2011). Iterative Reconstruction in X-ray Fluorescence Tomography Based on Radon Inversion. *IEEE Trans. Medical Imaging*, Vol. 30, Iss. 2, pp. 438-450

Natterer, F. (2001). Inversion of attenuated Radon transform. *Inverse Problem*, Vol. 17, pp. 113-119

Rust, G. F. & Weigelt, J. (1998). X-ray fluorescent computer tomography with synchrotron radiation. *IEEE Trans. Nucl. Sc*i., Vol. 45, Iss. 1, pp. 75-88

Schroer, C. G. (2001). Reconstructing x-ray fluorescence microtomograms. *Appl. Phys. Lett.*, Vol. 79, No. 12, pp. 1912-1914

Simionovici, A.; Chukalina, M.; Schroer, C.; Drakopoulos, M.; Snigirev, A.; Snigireva, I.; Lengeler, B.; Janssens, K. & Adams, F. (2000). High-resolution X-ray fluorescence microtomography of homogeneous samples. *IEEE Trans. Nucl. Sci.*, Vol. 47, Iss. 6, pp. 2736-2740

Simionovici, A.; Chukaline, M.; Gunzler, F.; Schroer, C.; Snigirev, A.; Snigireva, I.; Tummler, J. & Weitkamp, T. (2001). *Nucl. Instr. Meth. A*, 467–468, pp. 889-893

Takeda, T.; Maeda, T.; Yuasa, T.; Akatsuka, T.; , Ito, K.; Kishi, K.; Kazama, M.; Hyodo, K. & Itai, Y. (1995). Fluorescent scanning X-ray tomography with synchrotron radiation. *Rev. Sci. Instrum.*, Vol. 66, no. 2, pp.1471–1473

Takeda, T.; Akiba, M.; Yuasa, T.; Kazama, M.; Hoshino, A.; Watanabe, Y.; Hyodo, K.; Dilmanian, F. A.; Akatsuka, T. & Itai, Y. (1996). Fluorescent x-ray computed tomography with synchrotron radiation using fan collimator. *Proc. SPIE*, Vol. 2708, pp. 685–695

Takeda, T.; Kazama, M.; Zeniya, T.; Yuasa, T.; Akiba, M.; Uchida, A.; Hyodo, K.; Akatsuka, T.; Ando, M. & Itai, Y. (1998). Development of a monochromatic X-ray computed tomography with synchrotron radiation for functional imaging, In: *Medical Applications of Synchrotron Radiation*, M. Ando, C. Uyama, (Eds.), pp. 103-107, Springer-Verlag, Tokyo, Japan

Takeda, T.; Momose, A.; Yu, Q.; Yuasa, T.; Dilmanian, F. A.; Akatsuka, T. & Itai, Y. (2000). *Cell. Mol. Biol.*, Vol. 46, No. 6, pp. 1077-1088

Takeda, T.; Yu, Q.; Yashiro, T.; Zeniya, T.; Wu, J.; T.; Hasegawa, Y.Thet-Thet-Lwin; Hyodo, K.; Yuasa, T.; Dilmanian, F. A.; Itai, Y. & Akatsuka, T. (2001). Iodine imaging in thyroid by fluorescent X-ray CT with 0.05 mm spatial resolution. *Nucl. Instrum. Methods A*, Vol. 467–468, pp. 1318-1321

Takeda, T.; Yu, Q.; Yashiro, T.; Zeniya, T.; Wu, J.; Hasegawa, Y.; Thet- Thet-Lwin; Hyodo, K.; Yuasa, T.; Dilmanian, F. A.; Akatsuka, T. & Itai, Y. (2001). Iodine imaging in thyroid by fluorescent X-ray CT with 0.05 mm spatial resolution. *Nucl. Instrum. Methods A*, Vol. 467–468, pp. 1318-1321

Thet-Thet-Lwin; Takeda, T.; Wu, J.; Sunaguchi, N.; Murakami, T.; Mouri, S.; Nasukawa, S.; Huo, Q.; Yuasa, T.; Hyodo, K. & T. Akatsuka. (2007). Preliminary quantitative analysis of myocardial fatty acid metabolism from fluorescent X-ray computed tomography imaging. *J. Synchrotron Radiat.*, Vol. 14, No. 1, pp. 158-162

Thet-Thet-Lwin; Takeda, T.; Wu, J.; Huo, Q.; Yuasa, T.; Hyodo, K. & Akatsuka, T. (2008). Visualization of age-dependent myocardial metabolic impairment in cardiomyopathic model hamster obtained by fluorescent X-ray computed tomography using I-127 BMIPP. *J. Synchrotron Radiat.*, Vol. 15, No. 5, pp. 528-531

Takeda, T.; Wu, J.; Thet-Thet-Lwin; Huo, Q.; Yuasa, T.; Hyodo, K.; Dilmanian, F. A. & Akatsuka, T. (2009). X-ray fluorescent CT imaging of cerebral uptake of stable-iodine perfusion agent iodoamphetamine analog IMP in mice. *J. Synchrotron Radiat.*, Vol. 16, No. 1, pp. 57-62

Yu, Q.; Takeda, T.; Yuasa, T.; Hasegawa, Y.; Wu, J.; Thet-Thet Lwin; Hyodo, K.; Dilmanian, F. A.; Itai, Y. & Akatsuka, T. (2001). Preliminary experiment of fluorescent X-ray computed tomography to detect dual agents for biological study. *J. Synchrotron Radiat.*, Vol. 8, pp. 1030-1034

Yuasa, T.; Akiba, M.; Takeda, T.; Kazama, M.; Hoshino, A.; Watanabe, Y.; Hyodo, K.; Dilmanian, F. A.; Akatsuka, T. & Itai, Y. (1997). Reconstruction method for fluorescent x-ray computed tomography by least squares method using singular value decomposition. *IEEE Trans. Nucl. Sci.*, Vol. 44, pp. 54–62

Yuasa, T.; Akiba, M.; Takeda, T.; Kazama, M.; Hoshino, A.; Watanabe, Y.; Hyodo, K.; Dilmanian, F. A.; Akatsuka, T. & Itai, Y. (1997). Incoherent-scatter computed tomography with monochromatic synchrotron x ray: feasibility of multi-CT imaging system for simultaneous measurement-of fluorescent and incoherent scatter x rays. *IEEE Trans. Nucl. Sci.*, Vol. 44, pp. 1760-1769

Zeniya, T.; Takeda, T.; Yu, Q.; Hasegawa, Y.; Hyodo, K.; Yuasa, T.; Hiranaka, Y.; Itai, Y. Akatsuka, T. (2001). Integrated image presentation of transmission and fluorescent X-ray CT using synchrotron radiation, *Nucl. Instrum. Methods A*, Vol. 467–468, pp. 1326-1328

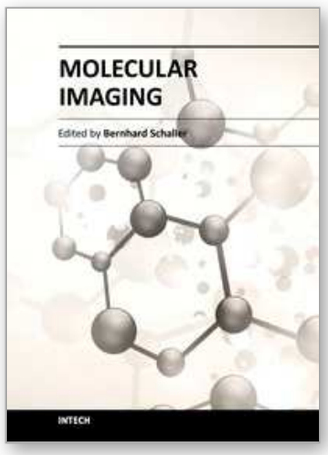

Molecular Imaging

Edited by Prof. Bernhard Schaller

ISBN 978-953-51-0359-2
Hard cover, 390 pages
Publisher InTech
Published online 16, March, 2012
Published in print edition March, 2012

The present book gives an exceptional overview of molecular imaging. Practical approach represents the red thread through the whole book, covering at the same time detailed background information that goes very deep into molecular as well as cellular level. Ideas how molecular imaging will develop in the near future present a special delicacy. This should be of special interest as the contributors are members of leading research groups from all over the world.

How to reference

In order to correctly reference this scholarly work, feel free to copy and paste the following:

Tetsuya Yuasa and Tohoru Takeda (2012). Fluorescent X-Ray Computed Tomography Using Synchrotron Radiation Towards Molecular Imaging, Molecular Imaging, Prof. Bernhard Schaller (Ed.), ISBN: 978-953-51-0359-2, InTech, Available from: http://www.intechopen.com/books/molecular-imaging/fluorescent-x-ray-computed-tomography-towards-molecular-imaging

INTECH
open science | open minds

InTech Europe
University Campus STeP Ri
Slavka Krautzeka 83/A
51000 Rijeka, Croatia
Phone: +385 (51) 770 447
Fax: +385 (51) 686 166
www.intechopen.com

InTech China
Unit 405, Office Block, Hotel Equatorial Shanghai
No.65, Yan An Road (West), Shanghai, 200040, China
中国上海市延安西路65号上海国际贵都大饭店办公楼405单元
Phone: +86-21-62489820
Fax: +86-21-62489821

IntechOpen